Original Article

Received: 2021-11-08
Accepted: 2021-12-02

BCCR
2021, No 3, Vol 13 :210-224
www.bccrjournal.com

^{18}FDG Production in a PET Imaging Using a Proton Flux Produced by the D-D Fusion Reaction

Nasrin Niknam[1], Seyedeh Nasrin Hosseinimotlagh[1*], Zohreh Parang[1]

1

1.Department of Physics, Shiraz Branch, Islamic Azad University, Shiraz, Iran

*Corresponding author:
Seyedeh Nasrin Hosseinimotlagh
Email: hosseinimotlagh@hotmail.com

ABSTRACT

Fluorine 18-deoxyglucose (^{18}FDG) is often used in Positron Emission Tomography (PET). PET imaging is one of the valuable tools used for cancer detection and management. PET growth is limited due to problems that depend on the production of Fluorine-18. Imaging results are strongly dependent on the information of nuclear reaction cross-section data. This study calculates the stopping power, R_{CSDA}, and the simulated and distributed absorbed dose of F-18, in water. We use the Geant4/Gate simulation and the Bethe-Bloch theory model to access these goals. The results of this simulation and this theory model agree with each other. The main point of this paper is the presentation of a theoretical approach to the production of Fluorine-18 by using protons production through the main nuclear fusion reaction D(d,p)T and the side fusion reaction ^{3}He(d,p)^{4}He uses helium-3 as a catalyzed.

Keywords: Fluorine-18, fusion, stopping power, absorbed dose, proton

INTRODUCTION:

Positron Emission Tomography (PET) is one of the advanced imaging systems with its unique ability to diagnose cancer, neurology, and cardiovascular diseases. Due to the very low half-life of radioactive materials used in PET, the production of radio drugs should be done by cyclotron in the vicinity of the PET center or close to it. Compared to an MRI scan or X-ray, the most significant advantage of a pet scan is showing the patient's body function compared to what appears healthy. In general, imaging is possible in two ways: 1. Anatomical (in MRI, CT) and 2. Functional (in SPECT, PET). In the case of anatomy, only the anatomy of the organs is visible. Therefore a lesion is detectable when its physical characteristics have changed (for example, the X-ray absorption coefficient in CT imaging or its proton density has changed in MRI imaging). If the physical characteristics have changed so much that it is visible in CT imaging, practically, it will be impossible to implement early and timely treatments. But in the functional imaging technique, the metabolic function of the tissue is visible before changing its physical characteristics. The metabolic changes have begun long before physical changes, and therefore functional imaging can provide early treatment before the disease progresses. Although MRI and CT functional are also available today, the sensitivity of these methods is still far below the ideal standards in nuclear medicine. PET imaging is based on the injection and distribution of the radio drug positron emission into the patient's body. Generally, the production of radio drugs positron emission is difficult, and their half-lives are also very short. Therefore, the drugs used in PET should be produced at the hospital and by cyclotron.
The patient rest for 1 to 1.5 hours (depending on the type of drug and tissue) to allow the drug to accumulate at the desired location. The drug in the body begins to decay. The positrons emitted before the collision with the substance and the loss of kinetic energy traveled a distance in the tissue called the positron range. Since positrons are unstable in nature alone and energy loss, they are combined with an electron and form positronium. The positronium is an unstable particle that disappears within a few microseconds. The mass converts to energy at that time called the annihilation effect. The amount of energy produced must be the same as the mass disappeared. Since the mass of an electron or positron equals 511 keV, two photons with an energy of 511 keV will be generated. Based on the momentum conservation, if we assume that the positron is combined with an electron after a complete stop (the momentum is zero), then the summation of momentum of each produced photon must be zero after the annihilation effect. Therefore, two photons move at 180 degrees angles to neutralize each other. This process involves a collision of an electron with a positron, and converting it into two gamma photons with a 511 keV is called the pair annihilation phenomenon. If the positron is not entirely stopped before its annihilation (combining with the electron), momentum is not zero, and therefore the final photon angle is less than 180 degrees. In any case, at particular energy for positron before being destroyed, the angle of the two photons is also constant. The imaging by injection of a radioactive matter is to find the site of radio drug accumulation in the tissue. But in the PET technique, instead of the positron accumulation site, its destruction site is visible (the final two-photon energy record site). If the positron range is higher, then the error will be greater. Therefore, the substances selected as radioactive drugs for injecting into a patient's body should contain positrons with low kinetic energy so that they cannot traverse large distances in the tissue (such as Fluorine-18). As already mentioned, positron emission tomography (PET) is potentially useful for monitoring the distribution of a dose deposited in the patient's body using proton therapy [1-8]. This method is based on the detection of the positron annihilation of γ rays following the decay of small amounts of positron emitters (typically ^{11}C , ^{13}N and ^{15}O) generated by the non-elastic nuclear reaction of protons with target nuclei under radiation. Treatment can be approved by comparing the PET images by detecting positron activity distribution with the predicted dose distribution used for treatment. The PET image reflects the distribution of energy deposited since the cross sections of the inelastic

nuclear reaction signal is along the beam's path. Still, at the Bragg peak, the greatest deposited energy of the proton through other interactions is reduced. However, by comparing the distribution of the measured radioisotope with PET, it is possible to confirm the effective dose with the efficiency of the predicted positron emitters from the program code therapy. The possibility of monitoring the proton therapy using PET by various groups has been investigated [2, 8]. However, due to the limitations of inelastic nuclear cross sections and precise simulation codes, most of the simulation studies performed in the past neglected the problem of low-proton energy. At the same time, Bragg's peak in monitoring is essential. In this paper, at first, we calculate the proton flux required for the production of fluorine 18 using fast ignition of the D-D fusion reaction via a ^{3}He catalyzed. Then, the cross-section and the rate production of fluorine-18, saturation coefficient, yield production of ^{18}F And followed by stopping power, CSDA range, absorbed dose of 18F in water using the Gate (Geant4 Application for Emission Tomography) and comparing it with the Bethe-Bloch model. We will examine its consistency. Also, we represent the steps in the synthesis and purification of FDG, especially irradiation of ^{18}O water with protons, to the cost reduction of FDG production.

2- Calculation of the proton flux produced by fast ignition of D-D fusion reaction via the ^{3}He catalyzed in ^{18}F production:

TIn 1994, Tabak et al. proposed a fast ignition method suitable for inertial fusion. Unlike the main hot spot ignition method, the compression and ignition processes are separated to reduce the hydrodynamic instabilities and achieve higher energy efficiency. In this method, the fuel capsule is compressed firstly at a low temperature by laser or ion beams to high areal density pR=2-3gcm^{-2} Then a time interval of 10-50ps is used from a laser beam with a power higher than 10^{18} W and a very short wavelength of 0.2 to ignition. [9-11] Many fusion researchers have developed the deuterium and tritium (D-T) fusion energy sources. Although the great D-T fusion reactivity has attracted fusion researchers, however, D-T burning has its serious problems because tritium inventory in nature is very low and must be artificially produced (using the reaction (n(^{6}Li,T)α). Providing adequate ratios of further tritium generation will pose a serious challenge to power plant design. In addition, tritium is a radioactive substance. In addition, the control of 14.1MeV neutrons from the D-T fusion reaction is difficult. But the product of the fusion reaction D-^{3}He is not a high-energy neutron. However, like tritium, ^{3}He is not abundant on the surface of the earth. However, the D-D fusion reaction may be the most interesting in eliminating the problem of high-energy neutrons related to the D-T reaction, although it has a relatively small fusion reaction cross section. [12, 13].The direct consequence of this reaction is that it reduces the amount of waste in fusion plasma that impedes ignition in laser fusion. The D-D cycle only uses deuterium as a fuel, which can even be extracted from seawater [9-11]. In a fusion reactor with D-D fuel, the fusion reactions occur from the following four channels:

$$D+D\rightarrow {}^{3}He(0.82MeV)+n(2.45MeV) \quad (1\text{-}a)$$
$$D+D\rightarrow T(1.01MeV)+p(3.02MeV) \quad (1\text{-}b)$$
$$D+T\rightarrow {}^{4}He(3.5MeV)+n(14.1MeV) \quad (2)$$
$$D+{}^{3}He\rightarrow {}^{4}He(3.6MeV)+p(14.7MeV) \quad (3)$$

reaction from the (1-a) and (1-b) channels occurs most likely, and the first channel produces ^{3}He.While the second channel produces tritium. Tritium and ^{3}He fuse with background deuterium (channels 2 and 3).The permissibility of tritium for fusion results in catalyzing the D-D fuel cycle. However, because the D-T reaction produces high-energy neutrons at 14.1 MeV. Which is difficult to control. Therefore, to solve this problem, we suggest that tritium decays before it performs a D-T fusion reaction and converts it to positron and ^{3}He. This ^{3}He, the product of the tritium decay, is replaced, and this results in the production of 22 MeV energy per D-D fusion reaction. This cycle is known as D-D fusion through the ^{3}He catalyzed. Assuming that tritium produced by D-D reaction and ^{3}He the product can be transferred to plasma; the rate of deuterium production is:

$$\frac{dn_D}{dt} = S_D - 0.5n_D^2 < \sigma v >_{DD,n} - 0.5n_D^2 < \sigma v >_{DD,p} - n_D n_T < \sigma v >_{DT} - n_D n_{3he} < \sigma v >_{D3He} - \frac{n_D}{\tau_p} \quad (4)$$

S_D=2.65×10^{22} is the source rate of deuterium production and τ_p is the particle confinement time. Production rates of ^{3}He for two states such as without and with catalyzed processes are given by the following equations:

$$\frac{dn_{He3}}{dt} = -\frac{n_{3He}}{\tau_p} + 0.5n_D^2 < \sigma v >_{DD,n} - n_{He3} n_D < \sigma v >_{DHe3} \quad (5)$$

(Without considering catalyzed process)

$$\frac{dn_{He3}}{dt} = -\frac{n_{3He}}{\tau_p} + 0.5n_D^2 < \sigma v >_{DD,n} + \frac{n_T}{\tau_p} - n_{He3} n_D < \sigma v >_{DHe3} \quad (6)$$

(Without considering catalyzed process)

$$\frac{dn_T}{dt} = 0.5n_D^2 < \sigma v >_{DD,p} - n_D n_T < \sigma v >_{DT} - \frac{n_T}{\tau_p} \quad (7)$$

These equations determine the fraction of non-deuterium ions, which is low than deuterium density. Finally, the proton, neutron, and alpha (^{4}He) rate equations and the balanced equation of energy production are written as follows, respectively:

$$\frac{dn_p}{dt} = -\frac{n_p}{\tau_p} + \frac{n_D^2}{2} < \sigma v >_{DD,p} + n_D n_{3He} < \sigma v >_{DHe3} \quad (8)$$

$$\frac{dn_n}{dt} = -\frac{n_n}{\tau_p} + \frac{n_D^2}{2} < \sigma v >_{DD,n} + n_D n_T < \sigma v >_{DT} \quad (9)$$

$$\frac{dn_{4He}}{dt} = -\frac{n_{4He}}{\tau_p} + n_{3He} n_D < \sigma v >_{DHe3} + n_T n_D < \sigma v >_{DHe3} \quad (10)$$

$$\frac{dE}{dt} = -\frac{E}{\tau_E} + Q_{D3He} n_D n_{3He} \langle \sigma \upsilon \rangle_{D3He} + Q_{DT} n_D n_T \langle \sigma \upsilon \rangle_{DT} + 0.5Q_{DD,p} n_D^2 \langle \sigma \upsilon \rangle_{DD,p} + 0.5Q_{DD,n} n_D^2 \langle \sigma \upsilon \rangle_{DD,n} - P_{bremsDD} - P_{bremsDHe3} - P_{bremsDT} \quad (11)$$

The required condition for neutralizing charge is: $n_D + n_T + 2n_{He} = n_e$ In addition, Q_{D3He}, Q_{DT}, Q_{DD}, $P_{bremsD3He}$, $P_{bremsDT}$, $P_{bremsDD}$ fusion reactions, and side reactions of D-T, D-^{3}He, respectively. So that:

$$P_{brems} = 4.85 \times 10^{-37} \times z_{eff} n_e^2 \sqrt{T} \left(\frac{W.m^3}{keV}\right) \quad (12)$$

And the reactivity of these fusion reactions is determined by the sigma-v parameter, which is defined as the product of the average cross-section into the relative velocity of the two nuclei. This averaging is performed on the function of the distributions of the velocities of the two nuclei, where the sigma-response parameter is generally defined as:

$$< \sigma v >= C_1 \theta e^{-3\mu} \sqrt{\mu / m_r c^2 T^3} \quad (13)$$

Where μ , θ and B_G follow the following relationships:

$$\begin{cases} \mu = \left(\frac{B_G^2}{4\theta}\right)^{\frac{1}{3}} \\ \theta = \frac{T}{\left[1 - \frac{T(C_2 + T(C_4 + TC_6))}{1 + T(C_3 + T(C_5 + TC_7))}\right]} \\ B_G = \pi \alpha Z_1 Z_2 \sqrt{2 m_r c^2} \end{cases} \quad (14)$$

It should be noted that the constant values of C_1 to C_7 are given in Table 1.

In Fig. 1, we plotted and illustrated the temperature vari-

Table 1. Constant values C_1 to C_7 in relation (14)

	T(d,n)^{4}He	D(d,n)^{3}He	D(d,p)T	^{3}He(d,p)^{4}He
C_1	1.17E-09	5.43E-12	5.66E-12	5.51E-10
C_2	1.51E-02	5.86E-03	3.41E-03	6.42E-03
C_3	7.52E-02	7.68E-03	1.99E-03	-2.03E-03
C_4	4.61E-03	0.00E+00	0.00E+00	-1.91E-05
C_5	1.35E-02	-2.96E-06	1.05E-05	1.36E-04
C_6	-1.07E-04	0.00E+00	0.00E+00	0.00E+00
C_7	1.37E-05	0.00E+00	0.00E+00	0.00E+00
$m_r c^{\wedge 2}$ (keV)	1124656	937814	937814	1124572

ations of <σv> for the fusion reactions described above. As can be seen from these graphs, the D-T reaction is most likely to occur, and the branch of the produced proton from the D-D reaction is the least. From the dynamic solution of equations 4 to 11, we obtain the density of each fusion particle and as well as the energy, gain of energy, and proton flux produced from the reaction, and the results are presented in Figs. 2 to 10 for two states of with/without catalyzed ^{3}He. As shown in Fig. 4, the density of deuterium fusion nuclei decreases with time. Because over time, the reactants have decreased. But calculations show that temperature variations do not affect the density of the fusion deuterium nuclei.

From Figs. 2 to 10, we conclude that the temperature and time variations of the produced particles, fusion energy, and proton flux with and without helium catalyzed except helium 3 in the case of helium catalyzed and deuterium are all similar. As the temperature rises at all times and at any temperature with gradually increasing time, it reaches a maximum value. It gradually decreases with time to reach the steady-state characteristic. But deuterium does not have such behavior because it burns as fuel consumed over time and gradually decreases to a steady-state characteristic value. But for helium-3, in the case of helium-catalyzed, with the enhancement of the temperature and time, it is increased at a constant time and after that time reaches the steady-state characteristic. The gain of fusion energy is: $G=E_{out}/E_{in}$ where E_{out} is the fusion energy released and E_{in} is the incident laser energy on the fuel. Our calculations give a maximum gain of approximately 25 at T = 100keV and $t=2.029\times10^{-10}$ s with E_{in}=0.1MJ taking into account the helium catalyzed, whereas without the helium catalyzed G is 6.5 at the same conditions. (See Figure 9).

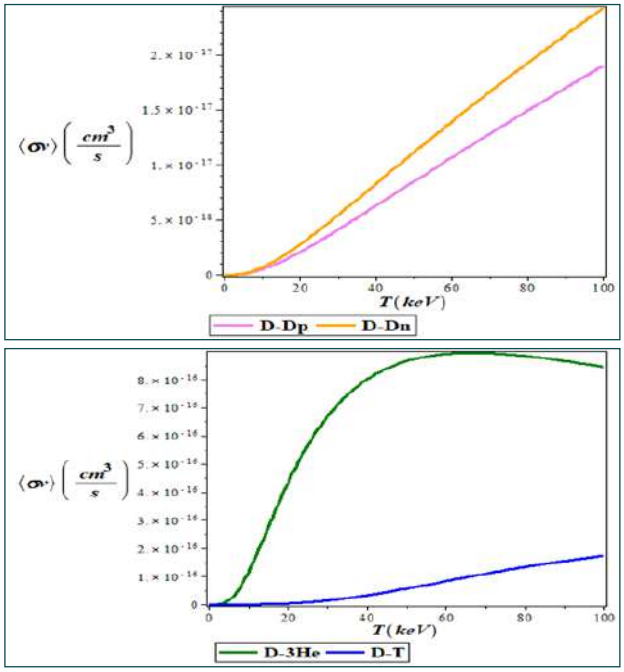

Figure.1. Temperature variations of <σv> for different fusion reactions

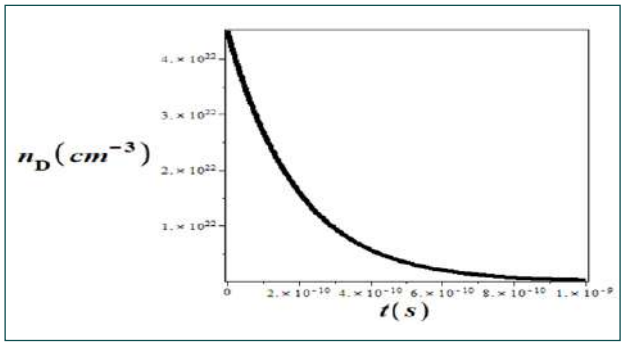

a: with ^{3}He catalyzed

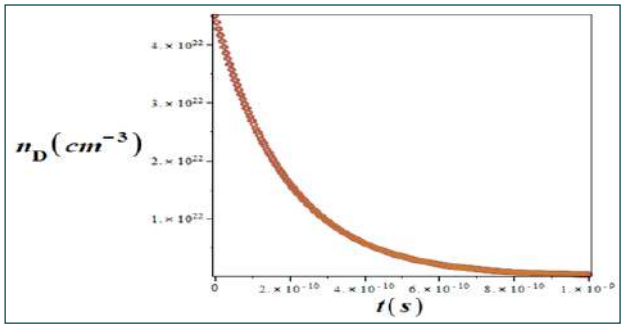

b: without ^{3}He catalyzed

Figure.2. time variations of deuterium particle density at the temperature range 0≤T(keV)≤100

3. Cross-section and production rate of Fluorine-18:

The rate of radionuclide production depends on several factors, including the magnitude of the cross-section reaction in terms of the energy function, the energy of the colliding particles, and the target thickness in terms of the number of nuclei per cm^2, which determine the energy of the output particles. The production rate of 18F is determined by the following relation:

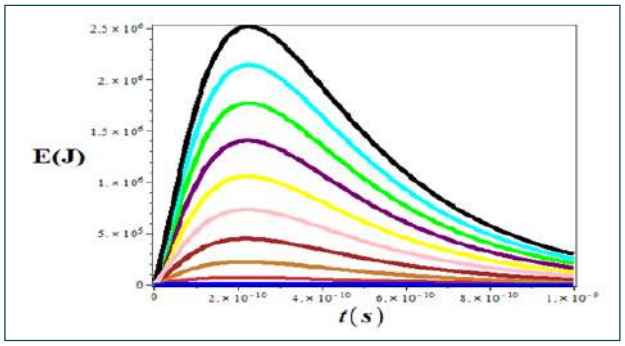

a: with ^{3}He catalyzed

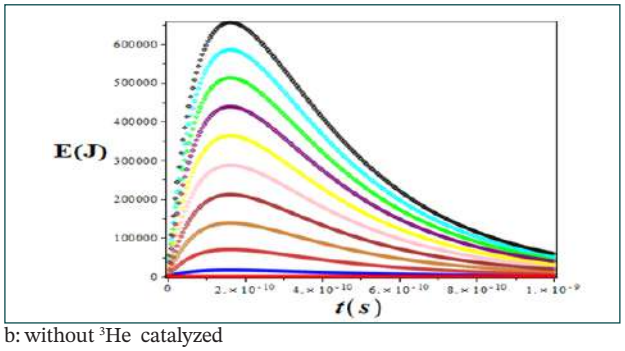

b: without ^{3}He catalyzed

Figure.3. time variations of produced fusion energy at the temperature range 0≤T(keV)≤100

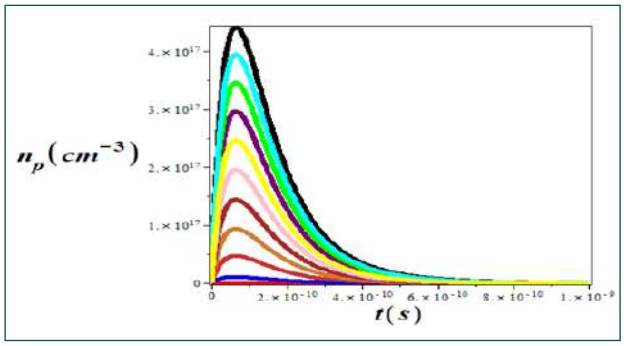

a: with ^{3}He catalyzed

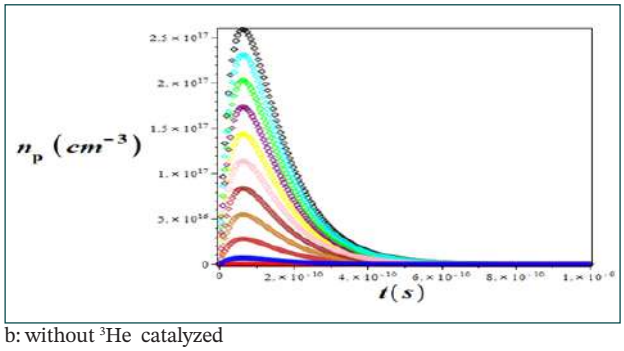

b: without ^{3}He catalyzed

Figure.5. time variations of produced proton particles at the temperature range 0≤T(keV)≤100

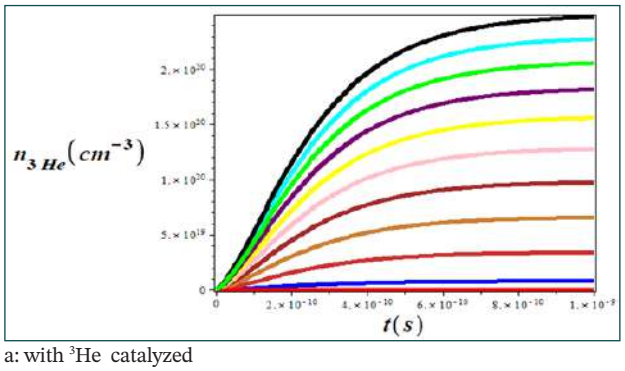

a: with ^{3}He catalyzed

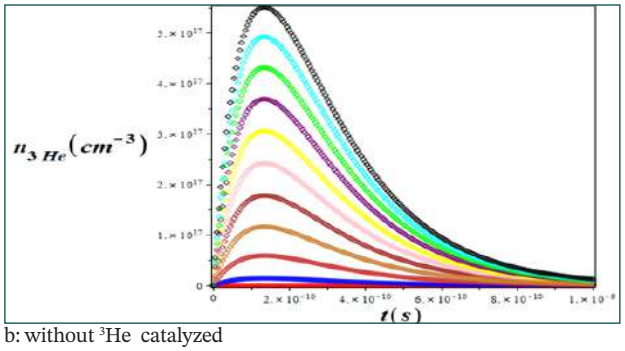

b: without ^{3}He catalyzed

Figure.4.time variations of produced ^{3}He particles at the temperature range 0≤T(keV)≤100

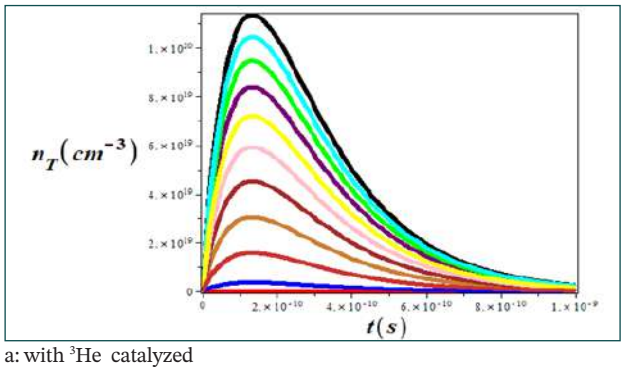

a: with ^{3}He catalyzed

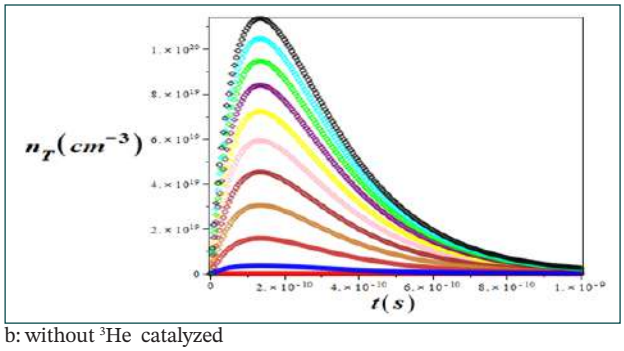

b: without ^{3}He catalyzed

Figure.6.time variations of produced tritium particles at the temperature range 0≤T(keV)≤100

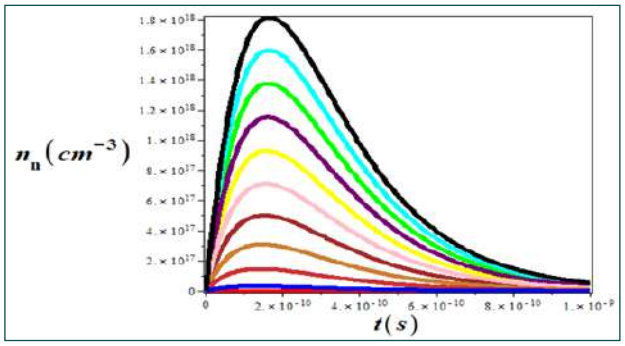

a: with ^3He catalyzed

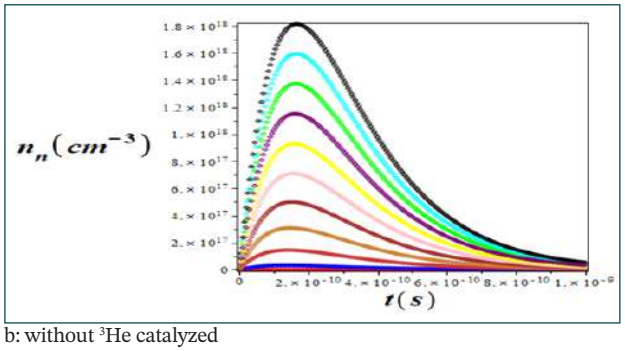

b: without ^3He catalyzed

Figure.7. time variations of produced neutrons particles at the temperature range 0≤T(keV)≤100

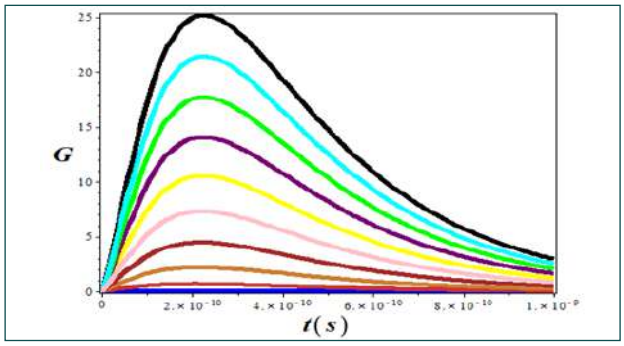

a: with ^3He catalyzed

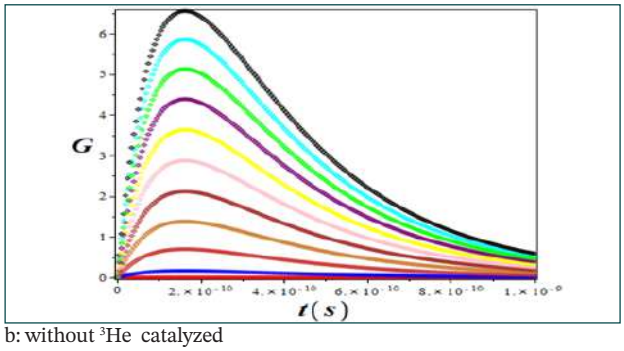

b: without ^3He catalyzed

Figure.9. time variations of energy gain at the temperature range 0≤T(keV)≤100

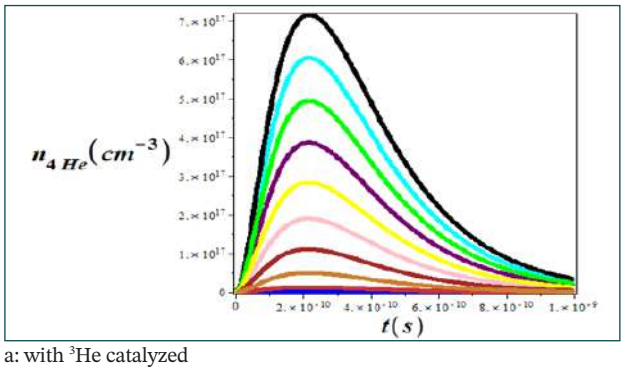

a: with ^3He catalyzed

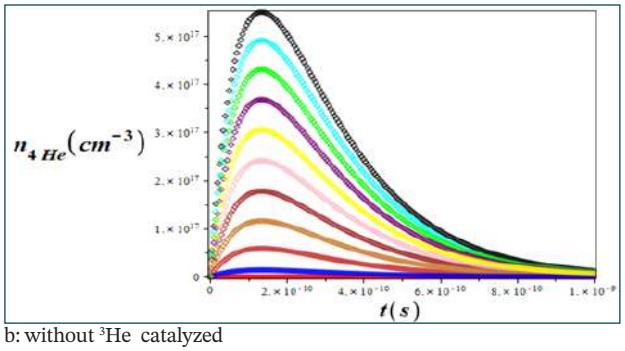

b: without ^3He catalyzed

Figure.8.time variations of produced(_^4)He particles at the temperature range 0≤T(keV)≤100

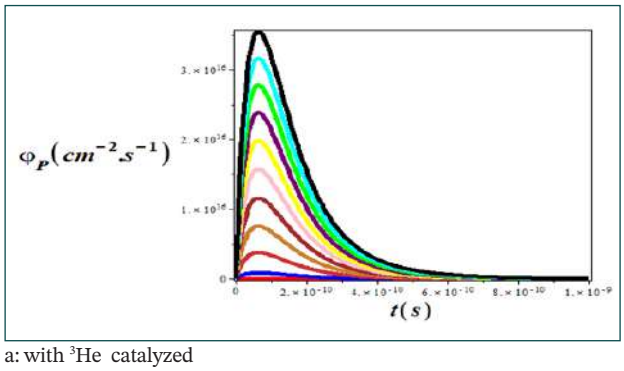

a: with ^3He catalyzed

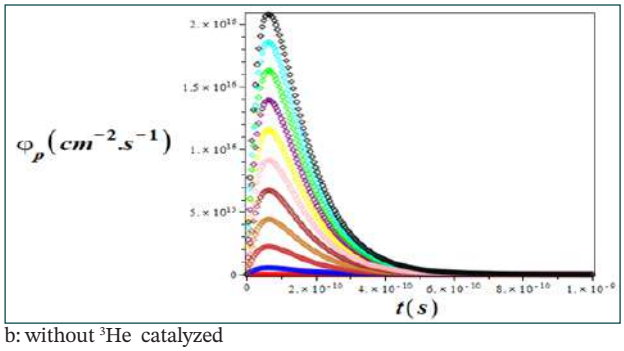

b: without ^3He catalyzed

Figure.10.time variations of proton flux at the temperature range 0≤T(keV)≤100

$$-\frac{dn}{dt} = R = nI(1 - e^{-\lambda t}) \int_{E_0}^{E} \frac{\sigma(E)}{dE/dx} dE \qquad (15)$$

Where R is the number of nuclei produced per second; n is the target thickness in units of nuclei per cm 2; I is the particle flux per second and corresponds to the beam flow; λ is the decay constant and is equal to (ln 2)/$T_{1/2}$; t is the time of irradiation in seconds; σ is the cross-section of reaction, or probability of interaction, whose unit is cm^2 and is a function of energy (see Fig. 1); E is the energy of the incident particles; x is the traveled distance by

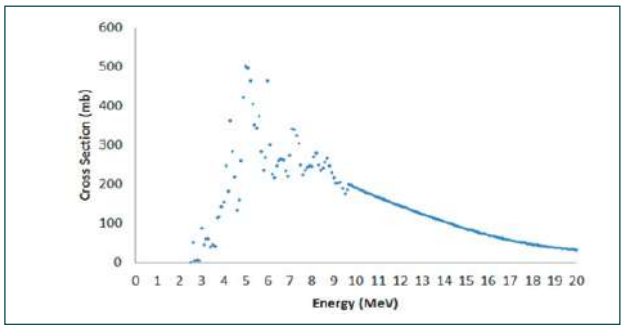

Figure.11. the variations of production of (_^18)F corresponding to the reaction ^{18}O(p,n)^{18}F

particle; dE⁄dx is the stopping power and ∫^{E}E0 is the integral that contains the initial energy to the final energy of the incident particles along the path.

4. Saturation coefficient:

At a shorter irradiation time, the product fraction is related to the saturation factor (S.F.), denoted by1-$e^{-\lambda t}$. Where λ is the nuclear decay constant, and t is the time of the bombardment. Irradiation with a half-life is equivalent to one half-life, leading to a 50% saturation. For practical reasons, irradiation rarely exceeds three half-lives (90% saturation). The practical production limits of a given radionuclide are determined by the isotope half-life. It is relatively easy to reach saturation to produce ^{15}O with a half-life of 2 minutes. But it is not reasonable for an irradiated target to produce ^{18}F to the saturation point because it requires too long irradiation times. In Fig. 12, we plotted the variations of saturation coefficient in terms of the ratio of the irradiation time to the half-life of the radionuclide produced by the ^{18}O(p, n)^{18}F reaction.

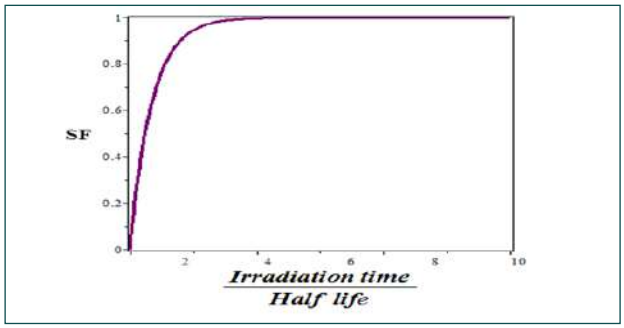

Figure.12. variations of saturation coefficient as a function of the ratio of the irradiation time to the half-life of the radionuclide produced by the ^{18}O(p, n)^{18}F reaction

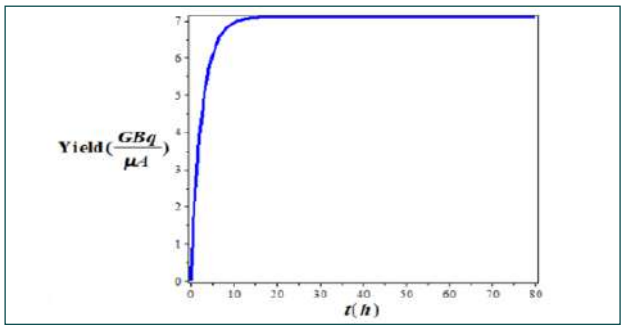

Figure.13. yield production of Fluorine- 18 in water versus time

5- Production yield of ^{18}F:

TSince the kinetic energy of the particle is slowly reduced by passing through a layer of thick target atoms, the production yield of ^{18}F on the thick target is given by the following relation:

$$\text{Yield} = \frac{3.76.10^9}{Z.M} \int_{E_{thershold}}^{E_{max}} \frac{\sigma(E)}{\frac{dE}{dx}} dE\left(1 - e^{-\lambda t}\right) {}^{MBq}/_{\mu A} \qquad (16)$$

Where Z is the atomic number of incident particle, M is the mass number of the target atoms $E_{thershold}$ to E_{max} is the energy interval, σ (E) is the cross-section at energy E, and dE/dx is the total stopping power at the target, as discussed below. λ is the decay constant, and t is the irradiation time (0 to 80 h). The unit of yield production is MBq⁄μA (due to the coefficient of 3.76*10^9.In Figure 13, we show the time variations of the yield production of Fluorine- 18 in water. It is seen that the yield production of Fluorine-18 gradually increases and reaches a steady state after 15 hours.

6. Stopping power, radiation yield, CSDA range, and ^{18}F absorbed dose in water:

Stopping power, CSDA range, and absorbed dose of ^{18}F in water are divided into two groups using Monte Carlo Gate / Geant-4 simulation code: Group 1: Heavy charged particles such as alpha and proton, Group II: Light charged particles such as electrons and positrons. Each group has specific interactions with biomaterials related to the mass difference between them. Isotope F-18 is a beta emitter with a half-life of 109.77 minutes used in medical imaging. This isotope is one of the anticancer drugs used to diagnose, regulate, and make "treatment decisions" for many cancer-related issues. Beta particles lose their energy in interaction with matter through two mechanisms. The first mechanism, so-called "collision loss", results in excitation (electrons move to higher energy levels) and ionization (unbound state) of matter where large scattering angles deflect heavy charged particles from their direct path. The second mechanism is the "radiative loss" that results in the emission of electromagnetic radiation (bremsstrahlung radiation) resulting from the acceleration of the particle. It usually does not matter for heavy charged particles because the magnitude of the bremsstrahlung radiation is proportional to the reciprocal square of the mass. The amount of energy transferred from the ionizing particle to biological targets is essential for tumor radiotherapy and should be accurately estimated. The stopping power depends on the type of radiation, the amount of energy, and the environmental characteristics that the particle passes through. Different studies have been done on the design of computational models to estimate this physical quantity. The stopping power formula involves the Coulomb interaction of heavy charged particles in the material. Also, there is another formula that calculates energy losses through bremsstrahlung radiation [15,16]. Development is continuing in this field, and the appropriate formula for the particle stopping power due to the Coulomb interaction has been defined by Tsoulfanidis et al. [17]. In this work, the collision stopping power properties of positrons in water in the energy range of 10 ev to 10 Kev are investigated using two formulas that incorporate the benefits of data obtained in PET imaging [17-19]. In another study, the modified stop power formula for low and medium energy positrons for different targets (water, Al, Cu, and Si) is presented [20]. The collision power or mechanism of radiation energy loss depends on the energy of the particles. In low-energy beta collisions, energy loss is predominant in radiation, while in high energy, radiation energy loss is the predominant mechanism that results in more bremsstrahlung radiation [18]. The risk of beta-particle bremsstrahlung radiation can be explained by the Y-radiation yield, defined as the average energy fraction that a beta particle radiates. The stopping power and the Continues Slowing Down Approximation Range, R_{CSDA}, (the path length of the irradiated particle in the target) related to the amount of absorbed dose D (energy loss per unit mass) is calculated can be calculated. The electron paths in the matter are similar to the positron paths in the matter, and the stopping power and range are almost the same for the equal initial energy. Monte Carlo simulation has a high degree of performance capable of covering all theoretical calculations of stopping power and cross-section. This improves limited problems in the field, such as the angles of scattering of radiation particles, the ionization and excitation process, and the change of energy dissipation of particles in the environment. This work aims to calculate and estimate the stopping power, R_{CSDA}, absorbed dose in water using Monte Carlo simulation. To understand this, the kinetic energy of the particles at the end of each annihilation process must be taken into account in the energy loss calculations for a particle. In this work, we simulate a positron F18 point source in the water at the center of a homogeneous environment (0,0,0) with a sufficient number of events. At the end of each annihilation process, the paths are presented with Cartesian coordinates (x, y, z) and energy loss values. The following is the Bethe-Bloch relativistic equation for calculating the stopping power of a light particle, which contains the sum of the two components of the collision and radiative stopping power [21,22]:

$$-\left(\frac{dE}{dx}\right)^{\mp}_{tot} = \left(-\left(\frac{dE}{dx}\right)^{\mp}_{coll}\right) + \left(-\left(\frac{dE}{dx}\right)^{\mp}_{rad}\right) \qquad (17)$$

The expression of the collision stopping power $-(\frac{dE}{dx})^{\mp}_{coll}$ is as follows:

$$-(\frac{dE}{dx})^{\mp}_{coll} = \frac{4\pi k^2 e^2}{mc^2\beta^2}\left[\ln\frac{mc^2\tau\sqrt{\tau+2}}{I\sqrt{2}}F^{\mp}(\beta)\right] \quad (18)$$

where

$$F^{-}(\beta) = \frac{1-\beta^2}{2} + \frac{1-\beta^2}{2(\tau+1)^2}\left[\frac{\tau^2}{8} - (2\tau+1)\ln 2\right] \quad (19)$$

It is about electrons and for positrons we have:

$$F^{+}(\beta) = \ln 2 - \frac{\beta^2}{24}\left[23 + \frac{14}{\tau+2} + \frac{14}{(\tau+2)^2} + \frac{14}{(\tau+2)^3}\right] \quad (20)$$

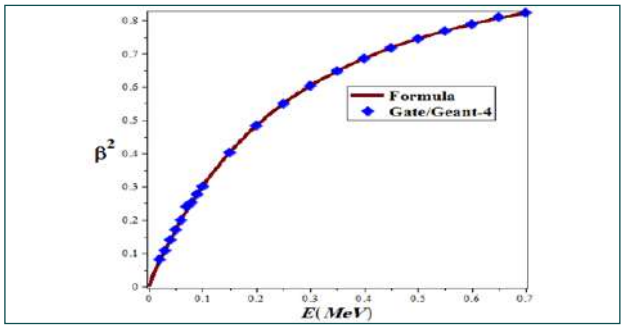

Figure.14. Comparison of β^2 variations in terms of particle energy in water at the range of 0.02≤E(MeV)≤0.7 using the Monte Carlo Gate / Geant-4 simulation code and the formula β^2=1-[(1+E/(mc^2))]^(-2)

For β^+, $\tau=E/(mc^2)$ is the kinetic energy of the beta particle, expressed in terms of the mass of the electron, and $\beta^2=v^2/c^2=1-(1+E/(mc^2))^{-2}$ where v is the particle velocity, c is the velocity of light in the vacuum, and k = Coulomb constant. In Fig. 14, a comparison of the variations of β^2 in terms of particle energy in water in the range of 0.02≤E(MeV)≤0.7 and using the Monte Carlo Gate / Geant-4 simulation code is shown.

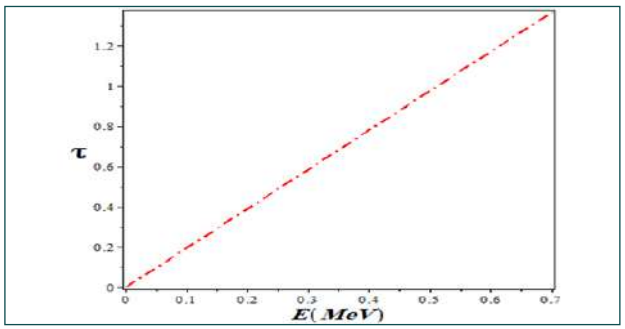

Figure.15. variations of the ratio of kinetic energy to resting positron energy (τ=E/(mc^2)) in the energy range of 0.02≤E(MeV)≤0.7 in water

As can be seen from Fig. 14, with increasing particle energy, β^2 is increasing, and the Monte Carlo Gate / Geant-4 simulation code and formula $\beta^2=1-(1+E/(mc^2))^{-2}$ are in good agreement. Figure 15 shows the graph of the positron kinetic energy variations in the energy range of 0.02≤E(MeV)≤0.7 in water.

As shown in Fig. 15, as E increases, the positron kinetic energy increases linearly. The average excitation energy for material is obtained using the following empirical formula:

$$I_i = 19.0\ eV, Z = 1 \quad (21)$$

$$I_i \cong 11.2 + 11.7Z\ eV, \quad 2 \le Z \le 13 \quad (22)$$

$$n\ln I = \sum_i N_i Z_i \ln I_i \quad (23)$$

Where: I = the average excitation energy in the environment in eV, n is the electron density of the matter, and Z is the atomic number. When we put these components in Equation 18, the formula for the stopping power effect is as follows:

$$-(\frac{dE}{dx})^{\mp}_{coll} = \frac{5.08\times10^{-31}n}{\beta^2}\left[\ln\frac{3.61\times10^5\tau\sqrt{\tau+2}}{I(eV)} + F^{\mp}(\beta)\right] \quad (24)$$

And the radiative stop power $-(\frac{dE}{dx})^{\mp}_{rad}$ is given by the following relation:

$$-\left(\frac{dE}{dx}\right)^{\mp}_{rad} = \left(\frac{dE}{dx}\right)^{\mp}_{coll} \times \left(\frac{dE}{800}\right) \quad (25)$$

In Fig. 16, we compare the variations of the collisional, radiative, and total positron mass stopping power in terms of particle energy in water in the range of 0.02≤E(MeV)≤0.7 using the Monte Carlo Gate / Geant-4 simulation code and the formulas used in Eqs.17, 24 and 25 are cited.

As can be seen from Fig. 16, the positron collision mass stopping power is decreased by increasing E, and its radiative stopping power is increased, and since positron collision mass stopping power is dominated by its radia-

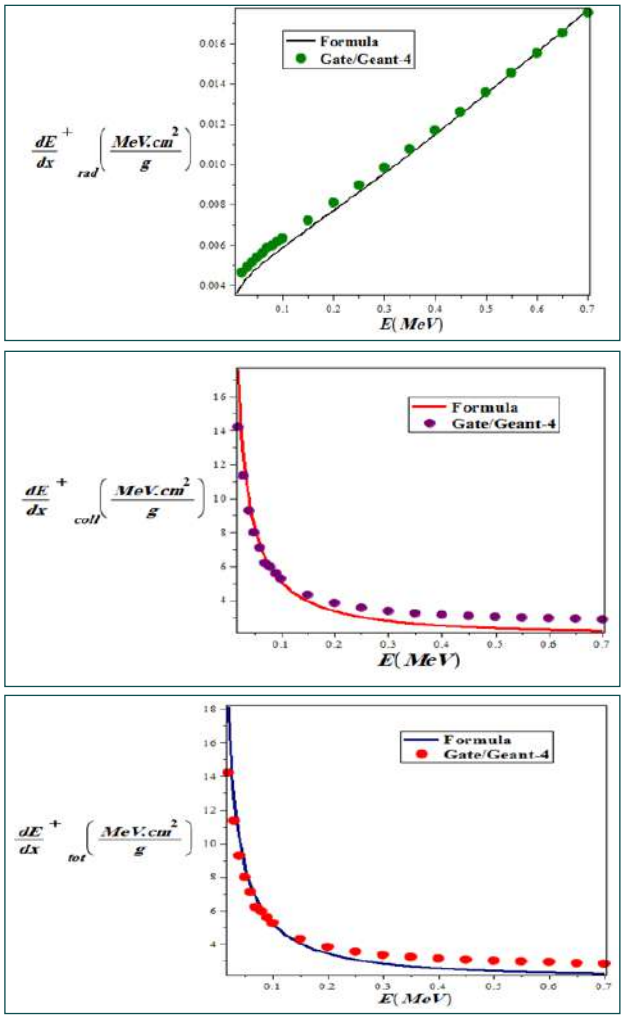

Figure.16. Comparison of mass-stopping power variations A: Collision B: Radiative C: Total positron versus particle energy in water in the range of 00.02≤E(MeV)≤0.7 using the Monte Carlo Gate / Geant-4 simulation code and the formulas presented in Equations 17, 24 and 25

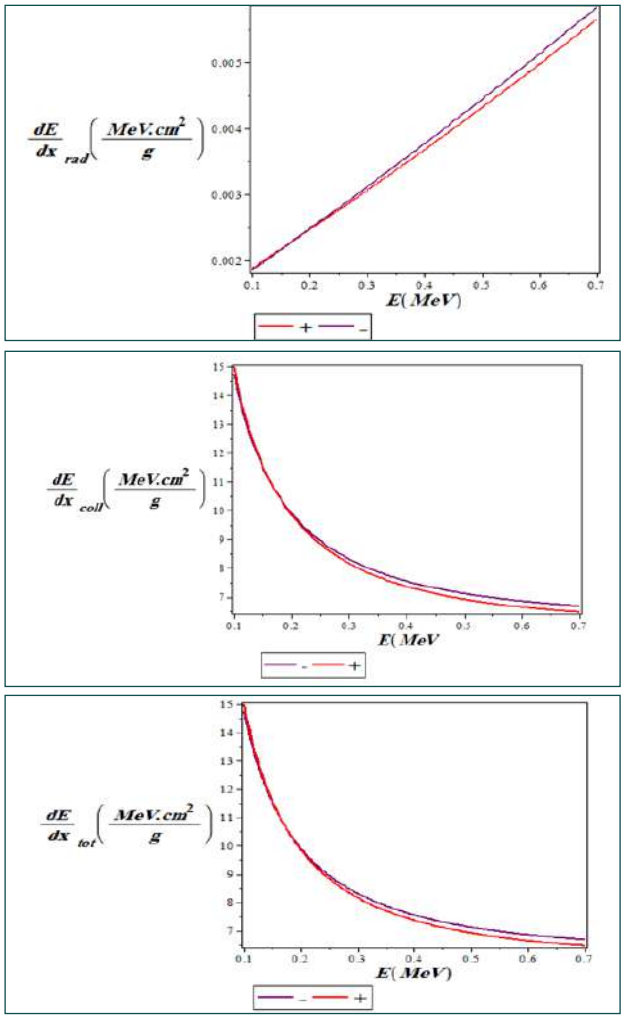

Figure.17. Comparison of mass-stopping power variations A: Collision B: Radiative C: Total positron and electron in terms of particle energy in water in the range of 0.02≤E(MeV)≤0.7 using the formulas presented in Equations 17 (Bethe-Bloch theory), 24 and 25

tive stopping power, such it decreases the total positron mass stopping power by increasing E. The results of the Monte Carlo Gate / Geant-4 simulation code and formulas 17, 24, and 25 are in good agreement. Also, to compare the mass-stopping power of the collision, radiative, and the whole positron and electron through the Bethe-Bloch theory, we draw Figures 17A, B, and C. It can be seen from this figure that at low energies, these powers are very close to the positron and the electron. Still, with increasing energy, they diverge, and the positron mass stops powerless than the electron.

For a beta particle of energy E in MeV passing through a material with atomic number Z the radiation yield (Y) is expressed as follows [23]:

$$Y \cong \frac{6 \times 10^{-4} ZE}{1 + 6 \times 10^{-4} ZE} \qquad (26)$$

In Fig. 18, we present the variations of the beta particle's radiation yield in terms of particle energy using Formula 26 and Monte Carlo Gate / Geante-4 simulation code. As can be seen from this figure, they are in good agreement at low energies and slightly distant at higher energies.

The mass stopping power $-(dE/\rho dx)_{total}^{\mp}$ (MeV.cm^2)/g) is obtained from the ratio of Equation 17 to the target den-

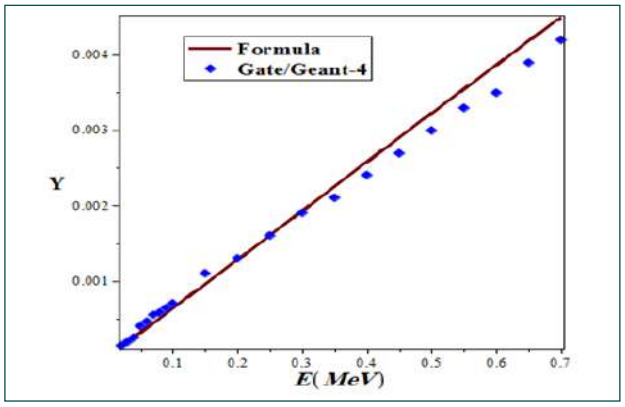

Figure.18. Comparison of beta particle radiation yield variations in terms of particle energy in water in the range 0.02≤E(MeV)≤0.7 using Formula 26 and Monte Carlo Gate / Geante-4 simulation code

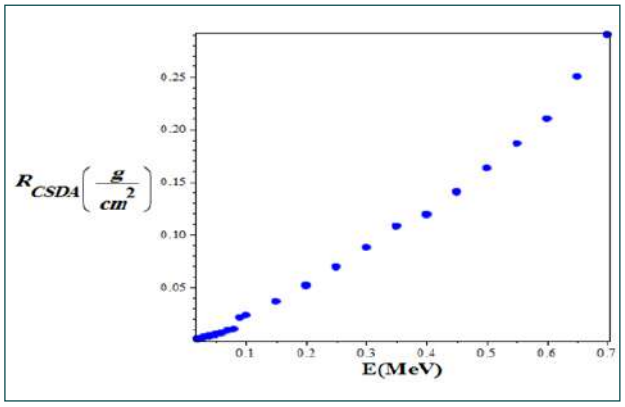

Figure.19. R_{CSDA} variations using Geant4 / Gate simulation code in terms of the kinetic energy of positive beta particle using Equation 27

sity. By integrating the inverse of $-(dE/\rho dx)_{total}^{\mp}$ ((MeV. cm^2)/g) from E (MeV) to zero the value of R_{CSDA} (g/cm^2) is obtained:

$$R_{CSDA} = \int_E^0 \frac{dE}{-\left(\frac{dE}{\rho dx}\right)_{total}^{\mp}} \qquad (27)$$

In Figure 19, we see that the R_CSDA variations using the Geant4 / Gate simulation code in terms of the kinetic energy of a positive beta particle. As can be seen by increasing the beta particle energy, the value of R_{CSDA} increases.

The absorbed dose D(MeV/g)is obtained by dividing R_{CSDA} to the target density to obtain the distance r (cm) that the particle travels in the medium [24]:

$$D = \frac{-\left(\frac{dE}{\rho dx}\right)_{total}^{\mp}}{4\pi\rho r^2} \qquad (28)$$

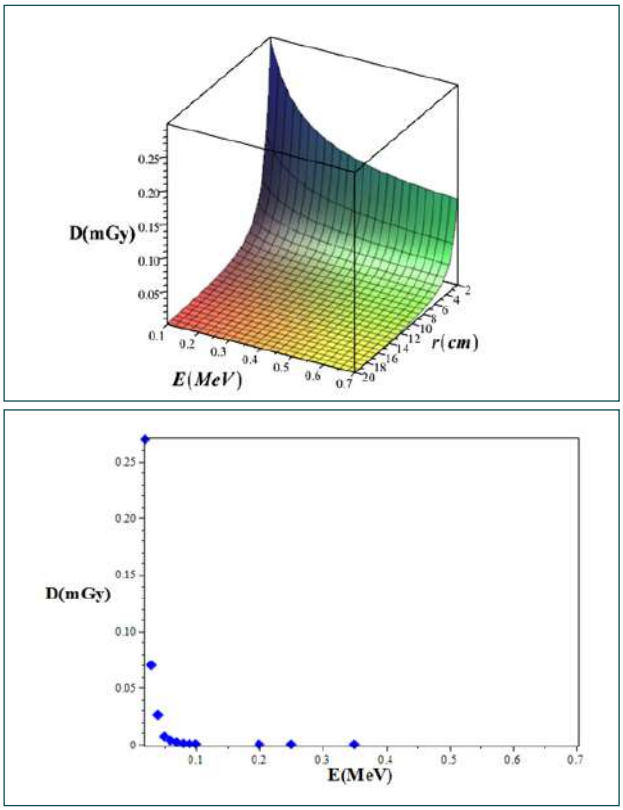

Figure.20. variations of A: 3D absorbed dose using Equ.28 B: Two-dimensional absorbed dose using Gate / Geant-4 simulation code in terms of particle energy and distance in water

Using Equation 28, we calculate the absorbed dose in water and plot its three-dimensional diagram of particle energy and distance variations in Fig. 20. As can be seen from the graph, the absorbed dose values of the computational method and the simulation method are consistent.

7-Steps in the synthesis and purification of FDG

The typical steps taken during FDG synthesis are summarized in the following:

Step 1: Irradiation of ^{18}F water with protons.

Step 2: Extraction of [^{18}F]fluoride from the H218O target.

Step 3: Drying of [^{18}F]fluoride.

Step 4: Labelling of the mannose triflate with the 18F.

Step 5: Removal of the protective acetyl groups by hydrolysis to form FDG.

Step 6: Purification and formulation of the final FDG product

Step 7: Sterilizing filtration.

Step 8: Sampling for quality control and quality assessment.
Step 9: Dispensing.
Step 10: Packaging and shipping.
Since protons are used in the first step for irradiating 18O water, we explain only this step, and the details of the other steps are found in Ref. [25].

8-Irradiation of 18O water with protons

The $^{18}O(p,n)^{18}F$ reaction with ^{18}O enriched water produces ^{18}F. Typical irradiation parameters include:(I) ^{18}O enrichment, typically >95%; (II) Chemical purity of ^{18}O enriched water, higher than 99.99%;(III) Target volume, ranging from 0.5 to 2.5 mL;(IV) Proton beam of 8–19 MeV;(V) Beam currents of 20–100 μA; (VI) Irradiation time from 30 min to 3 h. A detailed discussion of cyclotron targetry and radionuclide production is beyond the scope of this article but can be found in the literature, including Refs [26, 27].
The total amount of [^{18}F] fluoride generated depends on energy, beam current, and irradiation time. Other factors influencing total yield will be ^{18}O enrichment, chemical purity of enriched water, target material, target volume, and target design. One can expect approximately 111 GBq (3 Ci) of [18F]fluoride in a single target during one hour of irradiation with a 10–13 MeV proton beam at a beam current of 50 μA, and approximately 167 GBq (4.5 Ci) for a higher energy machine (14–19 MeV). The yield can be enhanced by increasing beam current and irradiation time and using dual targets. The chemical purity of enriched water is critical for longer irradiations with high beam currents. The benefit of longer irradiation needs to be carefully optimized, as the yield reaches a saturation point with long irradiations. Also, heat generated within a target limits the beam current that may be put onto a target. Nevertheless, with a customary useful FDG yield of >65%, several curies of FDG can be produced in a single irradiation/production cycle for in-house use and distribution to other PET centers. The oxygen-16 present in the target water leads to the production of ^{13}N through an (n,α) reaction, which is a radionuclidic impurity. Nitrogen-13 is a radionuclide decaying through positron emission with a half-life of 10 minutes, and hence a significant part of the 13N will decay during the synthesis of FDG, leaving trace amounts. Nitrogen-13 can appear in several chemical forms, including nitrate, nitrite, nitrogen, and ammonia, depending on target conditions. Also, depending on the method of synthesis and purification of FDG, some amount of ^{13}N may be present in the final product, resulting in a shorter measured half-life.
Since, at this stage, it is necessary to use protons in the energy range of 8-19 MeV and beam currents of 20–100 μA, this spark entered our minds that the occurrence of D-D fusion reactions and side reactions can be used as a source to generate electrical energy and also to produce 18FDG radioisotope for PET imaging. It should be noted that the cost of Positron Emission Tomography (PET) with [^{18}F]-fludeoxyglucose ((18)F-FDG) studies are mainly influenced by the price of the radiopharmaceutical, which may vary throughout Europe from 300 to 500 Euro per patient dose (370 MBq). Since that for producing of this radioisotope requires a cyclotron accelerator to accelerate the protons, which is expensive, therefore if the produced protons from the D.D. and D-3He fusion reactions are used with the energy of 3.02MeV and 14.7MeV, respectively, we will need smaller and less expensive cyclotron accelerators and as a result, will reduce the cost of final production of this radioisotope.

9-Conclusion

This paper presents a theoretical review of a novel method for the production of Fluorine-18 by employing proton production through the main fusion reaction D(d;p)T and side fusion $^{3}He(d,p)\,^{4}He$ using helium catalyzed. This study is also dedicated to developing a numerical analysis of stopping power, absorbed dose, and cross-sections related to positrons collisions with water. Such quantitative studies are beneficial for predicting the health status of patients at risk and scientifically understanding photons' annihilation in the environment. These results optimize patient exposure and effectively radiation the whole body without significantly reducing image quality.

REFERENCES

1. Basu S. Fundamentals of PET and PET/CT imaging. Ann. N. Y. Acad. Sci. 2011; 1228: 1–18.
2. Fischer BM. PET/CT is a cost-effective tool against cancer: synergy supersedes singularity. Eur J Nucl Med Mol Imaging. 2016;43: 1749–1752.
3. Marcu LG, Moghaddasi L and Bezak E. Imaging of Tumor Characteristics and Molecular Pathways with PET: Developments Over the Last Decade Toward Personalized Cancer Therapy. Int J Radiat Oncol .2018; 102: 1165–1182.
4. Cherry SR. Total-body imaging: transforming the role of positron emission tomography. Sci Trans Med. 2017; 9: 381-389.
5. Oelfke U. Proton dose monitoring with PET: quantitative studies in Lucite Phys Med Biol. 1996; 41: 177-186.
6. Parodi K, Enghardt W and Haberer T. In-beam PET measurements of β+ radioactivity induced by proton beams. Phys Med Biol. 2002; 47 :21-26.
7. Paans AMJ and Schippers JM. Proton Therapy in combination with PET as monitor: A feasibility study. IEEE Trans Nucl Sci. 1993; 40 :1041-1043.
8. Litzenberg D. On-line Monitoring and PET Imaging of the Positron-Emitting Activity Created in Tissue by Proton Radiotherapy Beams. Ph.D. Thesis, Univ. of Michigan. 1997.
9. Nakai S and Mima K, Reports on Progress in Physics. 2004; 67: 321–349.
10. Atzeni S and Meyer-Ter-Vehn J. The Physics of Inertial Fusion, Oxford Science Publications. 2004.
11. Cañadas M, Arce P, and Rato Mendes P. Validation of a small-animal pet simulation using gamos: A GEANT4-based framework. Phys Med Biol. 2011;56: 273– 288 .
12. Assie K, Gardin I, Vera P and Buvat I . Validation of the Monte Carlo simulator GATE for Indium 111 imaging. Phys Med Biol. 2005; 50:3113–3125
13. Bethe H. Bremsformel für Elektronen relativistischer Geschwindigkeit. Zeitschrift für Physik. 1932; 76: 293–299.
14. Ziegler, J. F. Stopping of energetic light ions in elemental matter. Journal of Applied Physics 1999; 85: 1249–1272.
15. Bloch F. Zur Bremsung rasch bewegter Teilchen beim Durchgang durch Materie. Annalen der Physik. 1933; 408:285–320.
16. Rohrlich F, Carlson BC. Positron–electron differences in energy loss and multiple scattering. Physical Review. 1954; 93:38–44.
17. Tsoulfanidis N. Measurement and detection of radiation. 2nd Edition. Taylor & Francis, Washington; 1995: 1–636.
18. Tanır G, Bölükdemir MH, Keleş S, Göker I. On the stopping power for low energy positrons. Chinese Journal of Physics. 2011; 50:1–9.
19. Gümüş H. New stopping power formula for intermediate energy electrons. Applied Radiation Isotopes. 2008; 66:1886–1890.
20. Gümüş H, Kabaday O, Tufan CM. Calculation of the stopping power for intermediate energy positrons. Chinese Journal of Physics. 2006; 44:290–296.
21. Krane K. Modern Physics. 2nd Edition. Department of Physics, Oregon University. John Wiley & sons Inc USA; 1996: 145.
22. Atoms JET. Radiation and Radiation Protection. 3rd Edition. Completely Revised and Enlarged Edition. WILEY-VCH Verlag GmbH & Co. KGaA, Weinheim Germany; 2007: 606.
23. Koch HW, Motz JW. Bremsstrahlung cross section formulas and related data. Reviews of Modern Physics. 1959; 31:920–55.
24. Prestwich WV, Nunes J, Kwok CS. Beta dose point kernels for radionuclides of potential use in radioimmunotherapy. Journal of Nuclear Medicine. 1989; 30:1036–46.
25. INTERNATIONAL ATOMIC ENERGY AGENCY, Cyclotron Produced Radionuclides: Guidance on Facility Design and Production of [18F]Fluorodeoxyglucose (FDG), 2012, VIENNA.
26. INTERNATIONAL ATOMIC ENERGY AGENCY, Cyclotron Produced Radionuclides: Principles and Practice, Technical Reports Series , 2009,No. 465, IAEA, Vienna

27. INTERNATIONAL ATOMIC ENERGY AGENCY, Cyclotron Produced
Radionuclides: Physical Characteristics and Production Methods, Technical Reports
Series , 2009, No. 468, IAEA, Vienna.